

Accessing Metal-Specific Orbital Interactions in C-H Activation using Resonant Inelastic X-ray Scattering

Ambar Banerjee^{1,*†}, Raphael M. Jay^{1,*†}, Torsten Leitner¹, Ru-Pan Wang², Jessica Harich², Robert Stefanuik¹, Michael R. Coates³, Emma V. Beale⁴, Victoria Kabanova^{4,‡}, Abdullah Kahraman^{4,§¶}, Anna Wach^{4,5}, Dmitry Ozerov⁴, Christopher Arrell⁴, Christopher Milne⁶, Philip J. M. Johnson⁴, Claudio Cirelli⁴, Camila Bacellar⁴, Nils Huse², Michael Odelius^{3*}, Philippe Wernet^{1,*}

¹Department of Physics and Astronomy, Uppsala University, 751 20 Uppsala, Sweden.

²Center for Free-Electron Laser Science, Department of Physics, University of Hamburg, 22761 Hamburg, Germany.

³Department of Physics, Stockholm University, AlbaNova University Center, 106 91 Stockholm, Sweden.

⁴Paul Scherrer Institute, CH-5232 Villigen PSI, Switzerland.

⁵Institute of Nuclear Physics, Polish Academy of Sciences, PL-31342 Krakow, Poland.

⁶European XFEL GmbH, 22869 Schenefeld, Germany.

*Corresponding authors: Ambar Banerjee, Raphael M. Jay, Michael Odelius, Philippe Wernet

Email: ambar.banerjee@physics.uu.se , raphael.jay@physics.uu.se , odelius@fysik.su.se , philippe.wernet@physics.uu.se

†These authors contributed equally to this work.

‡Present address: Department of Physics and Astronomy, Uppsala University, 751 20 Uppsala, Sweden.

§Present address: Stanford PULSE Institute, SLAC National Accelerator Laboratory, Stanford University, Menlo Park, CA 94025, USA.

¶Present address: Physical Sciences Division, Pacific Northwest National Laboratory, Richland, WA 99352, USA.

Abstract

Photochemically prepared transition-metal complexes are known to be effective at cleaving the strong C-H bonds of organic molecules in room temperature solutions. There is also ample theoretical evidence that the bidirectional charge-transfer between an incoming alkane C-H group and the transition metal is the decisive interaction in the C-H activation reaction. What is missing, however, are experimental methods to directly probe these interactions in order to reveal what determines reactivity of intermediates and the rate of the reaction. Here, we propose metal-specific and time-resolved valence-to-core resonant inelastic X-ray scattering (VtC-RIXS) at the transition metal L-edge as a method to provide a full account of the evolution of metal-alkane interactions during transition-metal mediated C-H activation reactions. For the model system cyclopentadienyl rhodium dicarbonyl (CpRh(CO)₂), we demonstrate with a combination of experiment and quantum chemical simulation how the Rh-centered valence-excited final states probed with VtC-RIXS directly reflect changes in donation and back-donation between the alkane C-H group and the transition metal as the reaction proceeds via its intermediates. Following the initial photo-triggered CO dissociation, we find substantial reduction in charge donation onto the metal and the resulting stabilization of metal-centered states as the alkane coordinates to the Rh center in a σ -complex intermediate. C-H bond cleavage in the final oxidative addition step is instead characterized by a substantial increase in back-donation as the new Rh-hydrogen and Rh-carbon bonds are formed. We benchmark and validate our simulations against experimental steady-state measurements. With our study, we predict the key spectral fingerprints for future time-resolved experiments of C-H activation reactions with CpRh(CO)₂ and related compounds.

We establish a new experimental observable for probing reactivity of C-H activation reactions as an example for how time-resolved VtC-RIXS serves to follow the valence electronic structure evolution along photochemical and photocatalytic reactions with transition metal complexes.

Introduction

Carbon-hydrogen (C-H) bonds are among the strongest chemical linkages in nature and thus inherently unreactive. Still, manipulating carbon-hydrogen bonds holds the key to numerous molecular transformations that are essential in organic and metal-organic synthesis within the context of “green chemistry”, the design of new pharmaceuticals or the transformation of low molecular weight hydrocarbons to high energy density liquid fuels (1). However, since C-H bonds lack considerable polarity, their manipulation via activation and functionalization is challenging due to significant energy barriers needed to be overcome under ambient conditions. One way of activating C-H bonds is using photo-triggered transition metal complexes (2, 3). Photochemical C-H activation with transition metal complexes, involves the dissociation of one or several ligands from the photo-excited transition metal complex in a room-temperature solution to generate a low-valent reactive metal center that then facilitates C-H bond cleavage in alkanes from solution. The most common metal complexes effectuating photoinitiated C-H activation are second or third row transition metal carbonyls and dihydrides, where the loss of a carbonyl or dihydride ligand creates a reactive metal center. The open coordination site at the metal then enables the binding of an alkane to form a so-called σ -alkane complex followed by subsequent C-H bond cleavage in an oxidative addition step by insertion of the metal into the C-H bond. Apart from this photoinduced C-H activation, there are numerous examples of C-H activation by transition-metal complexes which are not photoinitiated (4–6). Often, they involve so-called “agostic interactions” (7), a considerably different way of facilitating the breaking of the C-H bond compared to the metal-alkane interactions in a σ -complex (8).

Still, the various mechanisms of C-H activation by transition-metal complexes, be they photoinduced or not, can in fact be generally related to specific charge-transfer interactions between the metal d and C-H orbitals. The orbital symmetry (σ or π) and the direction of these interactions (metal to C-H donation or back-donation) can vary in incremental steps from case to case, thus forming a continuous range of charge-transfer mechanisms. Depending on the detailed nature of the orbital interactions and the overall charge transfer, a given complex can be placed in this continuum (9). Photoinitiated C-H activation via oxidative addition of an alkane to a transition metal constitutes a prominent mechanism within this spectrum.

The relevant charge-transfer interactions in C-H activation by transition metals were initially conceptualized on an orbital level by Saito & Hoffmann (10). It was proposed that C-H σ to metal-d (LMCT) charge donation and metal d to C-H σ^* (MLCT) charge back-donation act as the basic metal-alkane bonding and C-H bond cleavage interactions. C-H to metal donation was proposed to be essential in binding of the C-H bond to the metal center. Both C-H to metal charge donation and metal to C-H charge back-donation would then act in opposite directions but work in tandem to weaken the C-H bond and ultimately cleave it. The “two-way” charge transfer interactions between C-H and the metal (10, 11) act differently when binding the C-H group in a σ -complex compared to when cleaving the C-H bond and forming the final metal-carbon and metal-hydride bonds. It is therefore important to quantify the relative strength of these opposing modes of charge-transfer interactions for the different intermediates at the different stages of the reaction. Based on the above considerations, a generalized correlation diagram for how orbitals interact in the relevant intermediates in C-H activation by transition-metal complexes has been developed (10, 12). Computational approaches with energy decomposition schemes have attempted to estimate the relative strength of charge donation and back-donation. A general consensus, however, is lacking, because it is debated whether an unambiguous descriptor of the underlying orbital interactions actually exists. In addition, the means to experimentally access the hypothesized orbital interactions directly are missing to date. In terms of new experimental insight, it is access to the electronic structure of the σ -complex, the crucial intermediate in the activation process, that is of prime importance, since the transition-state, which is the point of focus of most computational studies, cannot be accessed experimentally. Time-resolved infrared spectroscopy has been used to identify reaction intermediates, including σ -complexes, by following IR marker modes (like the CO stretching frequency) (13–17). Relating the details of orbital-specific metal-alkane interactions in σ -complexes to the IR marker modes, however, is comparably indirect. Experimentally determining the

electronic structure properties, which drive C-H bond cleavage with transition metal complexes, by accessing the two-way charge-transfer interactions in an orbital-specific way and determining the relative strengths of the opposite components, thus remain challenging to date.

Using time-resolved X-ray absorption spectroscopy at the transition metal L-edge, we were recently able to observe the metal-alkane orbital interactions, which are operative in photoinduced C-H activation (18). We demonstrated, how with this atom-specific probe we could follow the evolution of orbital interactions and orbital populations as a function of time (19, 20). This enabled us to dissect the C-H σ to metal d charge donation and metal d to C-H σ^* (MLCT) charge back-donation in C-H activation (18). For photoinduced C-H activation with $\text{CpRh}(\text{CO})_2$ (where Cp is cyclopentadienyl) in octane solution, time-resolved X-ray absorption spectroscopy at the Rh L-edge gave access to the two-way charge-transfer interactions between Rh and the C-H group in the essential $\text{CpRh}(\text{CO})$ -octane σ -complex reaction intermediate. Metal L-edge XAS, however, is based on transitions of metal 2p core electrons to unoccupied molecular orbitals. The method is hence primarily sensitive to the unoccupied anti-bonding counterparts of the occupied bonding orbitals (21). For a full account of the two-way charge-transfer interactions and thus experimental access to the full correlation diagram for C-H activation by transition-metal complexes, it is therefore necessary to also probe the occupied orbitals (22, 23). Here, we demonstrate how valence-to-core resonant inelastic X-ray scattering (VtC-RIXS) at transition metal L-edges (20, 24–28) can be used to probe changes of orbital interactions in both, occupied and unoccupied orbitals. We show this by focusing on the decisive intermediates along the photoinitiated C-H activation pathway and we use $\text{CpRh}(\text{CO})_2$ to demonstrate our approach. By dissecting donation and back-donation interactions between Rh and an incoming C-H group on an orbital level we can now relate computationally established mechanisms and notions for reactivity in C-H activation by transition-metal complexes to the newly proposed experimental observables.

Probing C-H activation by $\text{CpRh}(\text{CO})_2$ using time-resolved VtC-RIXS at the Rh L-edge

C-H activation by $\text{CpRh}(\text{CO})_2$ is initiated by the photo-dissociation of a single CO moiety within 370 fs leading to the formation of a highly reactive undercoordinated singlet CpRhCO complex (18) (see schematic depiction of the overall process in Figure 1(a)). It has been conclusively established that CpRhCO binds with an alkane, both when performed in an argon matrix with methane or in an alkane solution (16, 18, 29–34). In octane solution, a σ -complex forms within 2 ps by the association of a C-H group to CpRhCO (18). σ -complex formation is followed by C-H activation via oxidative addition to the Rh center on nanosecond timescales, forming two new Rh-C and Rh-H bonds. $\text{CpRh}(\text{CO})_2$ serves as a model system for C-H bond activation, where electronic interactions are the predominant drivers, in contrast to other cases, where steric and cooperative effects dominate (31, 35). $\text{CpRh}(\text{CO})_2$ is therefore ideally suited as a benchmarking case to show how the orbital correlation diagram for C-H activation by transition-metal complexes can be made experimentally accessible with VtC-RIXS. Our proposed spectroscopic approach can then be extended to transition-metal systems also having varied degrees of reactivity as will be discussed at the end of this study.

The main orbital interactions here are the C-H σ to Rh 4d (LMCT) charge donation and the Rh 4d to C-H σ^* (MLCT) charge back-donation. C-H to Rh charge donation is responsible for σ -complex formation. Rh to C-H back-donation in contrast drives the oxidative addition step (10, 18) with a resulting transfer of charge density from Rh to the C-H moiety and, eventually, oxidation of the Rh center (see Figure 1(b)). We observed the progression of the reaction using time-resolved XAS at the Rh L_3 -edge by probing transitions of Rh 2p electrons into unoccupied molecular orbitals via Rh 2p \rightarrow 4d transitions thus accessing the anti-bonding analogs of the aforementioned orbital interactions (18).

Inspecting the valence molecular orbitals of $\text{CpRh}(\text{CO})_2$ reveals that the lowest unoccupied molecular orbital (LUMO) is predominantly a d_{xy} orbital, with the highest occupied molecular orbital (HOMO), HOMO-1, HOMO-2 and HOMO-3 being the d_{yz} , d_{z^2} , d_{xz} and $d_{x^2-y^2}$ orbitals, respectively (see Figure S1). These Rh 4d orbitals change and rehybridize across the reaction coordinate and, as we will show, the varying interactions of occupied MOs (specifically HOMO to HOMO-3) can be probed with Rh L-edge VtC-RIXS.

The VtC-RIXS process (denoted as RIXS hereafter) can be rationalized by the excitation of the system from the initial ground state (GS in Figure 1(c)) to an intermediate core-excited state (CES in Figure 1(c)) through the absorption of an incident X-ray photon, followed by inelastic scattering to a final valence-excited state (VES in Figure 1(c)). The RIXS process can therefore often be approximated by

an initial X-ray absorption step (as in X-ray absorption spectroscopy, XAS) followed by an X-ray emission step (as in X-ray Emission Spectroscopy, XES). By knowing the energy of the incident photon and measuring the energy of the scattered photon, their difference, and thus the energy being transferred to the system, can be determined (ΔE in Figure 1(c)). This energy transfer thus is a direct measure of the transition energies from the ground to valence-excited states. Resonant enhancement at the Rh L absorption edge makes the method specific to the Rh center. We further use the one-electron picture interpretation of the RIXS process to demonstrate sensitivity to specific molecular orbitals. The one-electron picture interpretation is well justified here because each transition between ground, core-excited and valence-excited states can be unambiguously assigned to transitions between Rh 2p, unoccupied and occupied molecular orbitals. This is illustrated for transitions between Rh 2p, HOMO and LUMO orbitals in Figure 1(d): The incident X-ray photon promotes an electron from the Rh 2p core orbitals to the unoccupied d_{xy} -LUMO. Subsequently, an electron from the HOMO can be thought to fill the Rh 2p core hole (the HOMO will have to have at least some Rh 4d character to have substantial intensity in the related dipole transition), leaving the system in a valence-excited final state of metal-centered (MC) character. The measured energy transfer (ΔE in Figure 1(c)) reflects the energy of the respective MC state and, within the one-electron picture interpretation, this energy transfer can also be approximately assigned to the energy of the HOMO-LUMO transition. Considering that other electrons from other occupied molecular orbitals with Rh 4d character (HOMO-1, HOMO-2, ...) can also fill the Rh 2p core hole, it is evident that this gives access to the HOMO-1, HOMO-2, to LUMO transition energies and thereby to the orbital-interaction energies involving all occupied orbitals accessible by p-d dipole transitions. Additionally, and again within the one-electron picture interpretation, the RIXS intensities of the HOMO, HOMO-1, HOMO-2, to LUMO transitions scale with the amount of Rh 4d character in the occupied molecular orbitals (mainly by orbital overlap). RIXS intensities therefore provide information on hybridization of the Rh 4d orbitals with surrounding ligand orbitals.

Figure 2(a) shows the measured steady-state XAS spectra and RIXS intensities of $\text{CpRh}(\text{CO})_2$ (for experimental details see Methods Section). The experimental data are compared to the calculated XAS spectra and RIXS maps. Calculations were done using the restricted orbital subspace time dependent density functional theory (TD-DFT) method (26, 27, 36) (see computational details in Methods Section). The simulated XAS and RIXS spectra reproduce all features of the experimental spectra. This is evidenced in a more quantitative evaluation in Figure 2(c), where cuts through the experimental and theoretical RIXS maps at the pre-edge peak in the Rh L-edge XAS spectrum at ~ 3005.8 eV are displayed. This pre-edge excitation corresponds to the transitions of Rh 2p electrons to the LUMO having prominent Rh 4d_{xy} character (18) (see Figure 1(d)). The RIXS spectrum taken at the XAS pre-edge at 3005.8 eV (see Figure 2(c)) therefore reflects the HOMO, HOMO-1, $\rightarrow 4d_{xy}$ (LUMO) transitions or, correspondingly, the energies of respective d-d (MC) valence-excited states. The simulated RIXS spectrum reproduces all relevant peaks in terms of both, energies and intensities. The calculated energy transfers are slightly overestimated, but their relative splittings are reproduced. The four transitions with highest intensities can be assigned to the four strong $4d_{yz}$, $4d_z^2$, $4d_{xz}$, and $4d_{x^2-y^2} \rightarrow 4d_{xy}$ orbital transitions (dark blue sticks in Figure 2(c), labeled as d_{yz} , d_z^2 , d_{xz} and $d_{x^2-y^2}$). This assignment is additionally verified using ab-initio methods (see Figure S1 in Supporting information for MOs). Based on the good agreement between calculated and measured RIXS maps of $\text{CpRh}(\text{CO})_2$, we proceed to tracking changes in Rh specific orbital interactions across the C-H activation reaction coordinate with Rh L-edge VtC-RIXS by predicting the XAS spectra and RIXS maps for the various reaction intermediates of $\text{CpRh}(\text{CO})_2$ upon C-H activation.

Rh L-edge RIXS signatures across the C-H activation pathway

The calculated Rh L-edge XAS spectra and RIXS maps of the essential intermediates along the C-H activation pathway of $\text{CpRh}(\text{CO})_2$ are displayed in Fig 3(a)-(d). We focus here on an analysis of the RIXS spectra taken at the XAS pre-edge peaks corresponding to Rh 2p \rightarrow LUMO transitions (dashed lines in Figures 3(a)-(d)), because the corresponding HOMO, HOMO-1, to LUMO transitions are most informative on the Rh-ligand frontier-orbital interactions.

We start with the free CpRhCO fragment in a singlet ground state and follow with the RIXS maps in Figure 3 what effects CO removal has on the frontier orbitals. Upon CO removal, the energy transfers of all RIXS features at the XAS pre-edge have considerably decreased by several eV along the energy-transfer axis compared to $\text{CpRh}(\text{CO})_2$ (compare Figs. 3(b) and 3(a)). These red-shifts reflect the overall reduction of covalent interactions of the frontier orbitals when a strongly bound ligand is removed. This is quantified by the cut through the RIXS map of CpRhCO at the XAS pre-edge (see Figure 3(e)).

Compared to the corresponding cut for $\text{CpRh}(\text{CO})_2$, CO removal decreases the energy transfers of the d_{yz} , d_z^2 , d_{xz} and $d_{x^2-y^2}$ RIXS peaks. These shifts correspond to how the $4d_{yz}$, $4d_z^2$, $4d_{xz}$, and $4d_{x^2-y^2} \rightarrow 4d_{xy}$ orbital transition energies from occupied orbitals to the LUMO decrease (correspondingly, these shifts reflect how energies of d-d (MC) states decrease when removing the CO from $\text{CpRh}(\text{CO})_2$). The red-shift of the lowest-energy d_{yz} RIXS peak from 3 eV in $\text{CpRh}(\text{CO})_2$ to 1 eV in CpRhCO (see Figure 3(e)) is particularly informative: It corresponds directly to the decrease of the HOMO-LUMO $4d_{yz} \rightarrow 4d_{xy}$ transition and hence reflects the destabilization of the HOMO (d_{yz}), or, more precisely, the reduction of the HOMO-LUMO energy separation. The HOMO (d_{yz}) orbitals in both $\text{CpRh}(\text{CO})_2$ and CpRhCO are associated with Rh 4d to CO (π^*) back-donation. Removal of CO from $\text{CpRh}(\text{CO})_2$ frustrates this interaction, thereby destabilizing the HOMO (d_{yz}) and stabilizing the LUMO (d_{xy}). The red shift of the d_{yz} RIXS peak ($4d_{yz} \rightarrow 4d_{xy}$ transition) quantifies this stabilization/destabilization. This is accompanied by an increase in intensity of that peak due to the increase of Rh d_{yz} character in the HOMO, when back-donation is frustrated upon CO removal (due to the dipole-allowed nature of the $4d_{yz} \rightarrow 2p$ transitions in the RIXS process). Note that, additionally, the pre-edge peak in the Rh L-edge XAS spectrum red-shifts from 3005.8 eV in $\text{CpRh}(\text{CO})_2$ to 3003.3 eV in CpRhCO (compare top panels in Figs. 3(a) and (b)). This corresponds to a decrease of the $2p \rightarrow \text{LUMO}$ ($4d_{xy}$) transition energy and reflects the stabilization of the LUMO orbital as CO is removed and a vacant coordination site is created at the Rh center in the free CpRhCO fragment (18). This is a manifestation of the creation of what has been termed “hole on the metal” by Hoffman et. al. (37).

Upon octane C-H coordination to the vacant site in the free fragment and thus formation of the CpRhCO -octane σ -complex, all d_{yz} , d_z^2 , d_{xz} and $d_{x^2-y^2}$ RIXS peaks at the XAS pre-edge shift back to higher energies (Figure 3(e)), indicating the recovery of covalent interactions at the Rh center to a certain degree. Specifically, C-H to Rh coordination shifts the HOMO-LUMO $4d_{yz} \rightarrow 4d_{xy}$ transition (d_{yz} RIXS peak) back from 1 eV in the free CpRhCO fragment to slightly more than 2 eV in the σ -complex (Figure 3(e)). The related recovery of the HOMO-LUMO energy separation directly reflects the increase of underlying charge donation and back-donation interactions. The emerging Rh 4d to C-H σ^* (MLCT) charge back-donation stabilizes the HOMO (accompanied with some increase in C-H σ^* character in the HOMO and a corresponding slight decrease of the intensity of the d_{yz} RIXS peak). The new or increased C-H σ to Rh 4d (LMCT) charge donation destabilizes the “hole on the metal” LUMO orbital in the CpRhCO -octane σ -complex compared to the free CpRhCO fragment. Correspondingly, the XAS pre-edge resonance shifts back as well from 3003.3 eV in CpRhCO to 3004.4 eV in CpRhCO -octane (see Figure 3(b) and (c) top).

Importantly, we note that the energies of the d_{yz} RIXS peaks (HOMO-LUMO $4d_{yz} \rightarrow 4d_{xy}$ transition energies) amount to only slightly more than 2 eV in the σ -complex compared to 3 eV in $\text{CpRh}(\text{CO})_2$ (Figure 3(e)). This difference suggests a smaller HOMO-LUMO energy separation in CpRhCO -octane compared to $\text{CpRh}(\text{CO})_2$. This is a direct manifestation of the weaker Rh 4d to C-H σ^* back-donation in CpRhCO -octane compared to the Rh 4d to CO π^* back-donation in $\text{CpRh}(\text{CO})_2$ (a corresponding effect on the LUMO orbitals of the two structures can be seen in the difference in Rh L-edge XAS pre-edge resonance energies). Our Mullikan population analysis of orbitals shows that the Rh 4d character of the HOMOs for CpRhCO -octane and $\text{CpRh}(\text{CO})_2$ amount to 38.1% and 22.5%, respectively. This difference can be related to the smaller overlap of Rh 4d and C-H σ^* orbitals in CpRhCO -octane compared to the overlap of Rh 4d and CO π^* orbitals in $\text{CpRh}(\text{CO})_2$ and a correspondingly smaller degree of hybridization. In RIXS, the difference in 4d character can be directly observed from the higher intensity of the d_{yz} peak in CpRhCO -octane compared to $\text{CpRh}(\text{CO})_2$ (see Figure 3(e)).

Oxidative addition of the C-H bond to the Rh center in the final step of the reaction pushes the C-H group closer to the Rh center, thereby increasing both C-H σ to Rh $4d_{xy}$ donation and Rh $4d_{yz}$ to C and H σ^* charge back-donation. As Figure 3(e) clearly shows, oxidative addition shifts all d_{yz} , d_z^2 , d_{xz} and $d_{x^2-y^2}$ RIXS peaks at the XAS pre-edge to higher energies compared to the CpRhCO -octane σ -complex (correlating with the increase of covalent interaction in the final hydride product CpRhCO-R-H). The d_{yz} RIXS peak, in particular, red shifts from slightly more than 2 eV in CpRhCO -octane to above 4 eV in CpRhCO-R-H (Figure 3(e)). This notable shift of the HOMO-LUMO $4d_{yz} \rightarrow 4d_{xy}$ transition to an energy even higher than in $\text{CpRh}(\text{CO})_2$ (3 eV) is reflective of a substantial increase of Rh $4d_{yz}$ to C and H σ^* back-donation and a related stabilization of the HOMO (d_{yz}) when the metal hydride with covalent Rh-C and Rh-H bonds is formed. The d_{yz} RIXS peak also significantly decreases in intensity, resulting in it no longer being identifiable as a separate peak as in $\text{CpRh}(\text{CO})_2$, CpRhCO , and CpRhCO -octane (see Figure 3(e)). This directly points to the significant loss of $4d_{yz}$ character in the HOMO as Rh $4d_{yz}$ to C and H σ^* charge back-donation increase. Our Mullikan population analysis reveals that the 4d character

of the HOMO drops from 38.1% in CpRhCO-octane to 15.5% in CpRhCO-R-H and much lower than the 22.5% in CpRh(CO)₂. We also note that the overall energy spread, over which the d_{yz} , d_z^2 , d_{xz} and $d_{x^2-y^2}$ RIXS peaks are distributed, decreases from around 2 eV in CpRh(CO)₂, CpRhCO and CpRhCO-octane to around 1 eV in the final metal hydride CpRhCO-R-H (Figure 3(e)). An explanation of this is given below.

As a final note, the strong C and H σ to Rh $4d_{xy}$ donation in the final metal hydride destabilizes the LUMO (while the Rh $4d_{yz}$ to C and H σ^* charge back-donation stabilizes the LUMO+1). Consistently, the pre-edge XAS peak shifts from 3004.4 eV in the CpRhCO-octane σ -complex to 3006.6 eV in CpRhCO-R-H (Figure 3(c) and (d), top) (notably to a higher incident energy as in CpRh(CO)₂ where it is at 3005.8 eV due to the stronger C-H versus CO ligand to Rh charge donation).

Motivated by the stringent consistency between changes in orbital interactions and changes in the RIXS spectra at the XAS pre-edge across the reaction coordinate, we now turn to a more explicit prediction of experimental observables and, alongside, a more detailed analysis of the final oxidative addition step of the reaction. In future pump-probe experiments, the ground-state CpRh(CO)₂ species will be photoexcited and the emerging reaction intermediates will be measured against a background of unexcited CpRh(CO)₂. For measurements of the CpRhCO free fragment and of the CpRhCO-octane σ -complex, the calculated RIXS maps and spectra in Figure 3 serve as good predictions, because their XAS pre-edge resonances are well separated from the absorption edges of CpRh(CO)₂. By tuning the incident energies to the easily identifiable respective pre-edge resonances, the RIXS spectra of CpRhCO and CpRhCO-octane can be straightforwardly measured. For the final CpRhCO-R-H metal hydride product, though, the situation is more complicated because its Rh L-edge XAS spectrum as well as RIXS map strongly overlap with the corresponding spectral features of ground-state CpRh(CO)₂ (Figure 3(a), (d) and (e)). To isolate detailed changes in electronic structure upon metal hydride formation compared to un-excited CpRh(CO)₂, we therefore analyze RIXS difference maps, where RIXS intensities of the ground-state CpRh(CO)₂ species (as a reference) are subtracted from the RIXS intensities of the final metal hydride product. This approach is commonly applied in pump-probe experiments and was shown before to render adequate RIXS intensities of reaction intermediates (20). The more subtle changes in RIXS intensities are emphasized and the information needed to relate changes in RIXS intensities to an overall orbital correlation diagram for the oxidative addition step is revealed.

The calculated RIXS difference maps for the CpRhCO-octane σ -complex and the metal hydride product CpRhCO-R-H are shown in Figure 4(a) and (b) (for completeness, equivalent data of CpRhCO are shown in Figure S2). Cuts through these difference maps (rendering RIXS difference spectra) are compared in Figure 4(c) for the two species and reveal the valence electronic-structure changes along the reaction coordinate of oxidate addition in C-H activation. These differences reflect the peak shifts discussed above and, in addition, make visible the more subtle changes in peak intensities (changes in Rh 4d character in the occupied $4d_{yz}$, $4d_z^2$, $4d_{xz}$ and $4d_{x^2-y^2}$ orbitals). The RIXS difference map of CpRhCO-octane can be almost exclusively described by the depletion of ground-state CpRh(CO)₂ intensities (compare negative, blue-marked, intensities in Figure 4(a) with the RIXS map of CpRh(CO)₂ in Figure 3(a)) and the shifted RIXS intensities of CpRhCO-octane (compare positive, red-marked, intensities in Figure 4(a) with the RIXS map of CpRhCO-octane in Figure 3(b)). The corresponding RIXS difference spectrum of CpRhCO-octane at the XAS pre-edge shown in Figure 4(c) thus almost exclusively exhibits positive intensities only (with some negative intensities due to spectral overlap of RIXS intensities in the RIXS maps of CpRhCO-octane and depleting CpRh(CO)₂ at energy transfers above 5-6 eV).

The RIXS difference map of the final CpRhCO-R-H in Figure 4(b) is more complex as expected. Intensities at zero energy transfer reflect the blue shift of the XAS pre-edge in CpRhCO-R-H compared to CpRh(CO)₂ (see the opposite pattern in Figure 4(a) at zero energy transfers due to the opposite red shift of the XAS pre-edge in CpRhCO-octane compared to CpRh(CO)₂). A cut at the XAS pre-edge (at 3006.6 eV, Figure 4(c)) clearly shows strong intensity modulations in both, positive and negative directions (in contrast to the CpRhCO-octane RIXS difference spectrum). The negative-intensity feature at 3-4 eV for CpRhCO-R-H reflects the aforementioned reduced intensity of the d_{yz} RIXS peak in CpRhCO-R-H with respect to CpRh(CO)₂ and the correspondingly lower Rh 4d character in the $4d_{yz}$ HOMO in CpRhCO-R-H compared to CpRh(CO)₂. This depletion of Rh 4d character is a clear indication

of oxidation as it can be interpreted as an increase in Rh 4d to C-H σ^* charge back-donation to the point of the metal getting oxidized from Rh(I) to Rh(III).

Our analysis offers a unique way to motivate, verify and extend the orbital correlation diagrams for C-H activation by transition-metal complexes proposed by Ess and coworkers (12). Figure 4(d) shows the correlation diagram for the oxidative addition step, which we extract from our calculations and directly correlate with the calculated RIXS intensities and energies. The changes in energies and hybridization of the most relevant unoccupied molecular orbitals, i.e., of LUMO, LUMO+1, LUMO+2, LUMO+3, were reported earlier based on our combination of calculations and measured XAS spectra (as indicated in Figure 4(d), they are fully consistent with the changes reported here for the occupied orbitals) (18). Using RIXS, we can additionally track the changes in energies and hybridization of the occupied orbitals. The changes in the Rh $4d_{yz}$ HOMO discussed so far, are depicted in our extended correlation diagram in Figure 4(d). With future time-resolved Rh L-edge RIXS experiments, these changes and the related correlation diagram will become accessible experimentally. Specific intensity variations of the other RIXS peaks relating to HOMO-1 to HOMO-3 are less clear because shifts in the peaks strongly interplay with variations in peak intensities. Still, when comparing the RIXS difference cuts at the XAS pre-edges of the CpRhCO-octane σ -complex and of the final CpRhCO-R-H product in Figure 4(c), we can state that CpRhCO-R-H exhibits stronger negative intensities. This reduced RIXS intensity reflects an overall decrease of Rh 4d character in the Rh-centered occupied orbitals, which are involved in formation of the new covalent Rh-C and Rh-H bonds.

Inspection of the molecular orbitals of CpRhCO-R-H (see. Figure S3) indeed shows that the $4d_{x^2-y^2}$ (HOMO-3 in CpRhCO-octane and CpRhCO-R-H) and $4d_z^2$ (HOMO-1 in CpRhCO-octane and HOMO-2 in CpRhCO-R-H, see Figure 4(d)) hybridize with the C sp^3 and H s orbitals as they are favorably oriented in space to form the corresponding bonding overlaps for the new Rh-C and Rh-H bonds (Figure 4(d)). We also find that in CpRhCO-R-H, the HOMO-1 and HOMO-2 stabilize more than HOMO-2 and HOMO-4, resulting in an energetic cross-over between the HOMO-2 and HOMO-3. This behavior also explains the decrease in the earlier-mentioned energy spread of d_{yz} , d_z^2 , d_{xz} and $d_{x^2-y^2}$ RIXS peaks. At the same time, the Rh character in these orbitals significantly decreases. Our Mulliken population analysis yields a decrease from 72.9% to 60.9% for $4d_{x^2-y^2}$ HOMO-3 and from 77% to 34% for $4d_z^2$ HOMO-1/HOMO-2 when going from CpRhCO-octane to CpRhCO-R-H. The $4d_{xz}$ (HOMO-2 in CpRhCO-octane and HOMO-1 in CpRhCO-R-H, see Figure 4(d)), finally, is also stabilized upon oxidative addition and, accordingly, significantly loses Rh 4d character as the covalent bonds are formed. According to the Mulliken population analysis, the Rh 4d character in the $4d_{xz}$ orbital decreases from 80.8% to 59%.

These quantum-chemical predictions directly relate to experimental RIXS observables, as we show, and can be used to construct and conceptualize the entire correlation diagram in Figure 4(d). By explicitly considering covalent interactions involving all occupied 4d orbitals, we extend upon previous theoretical concepts, which were purely based on charge donation and back-donation interactions. RIXS will also enable revealing how varying degrees of C-H σ^* to metal-d (LMCT) charge donation and metal-d to C-H σ^* (MLCT) charge back-donation, as induced by different spectator ligands for instance, influences the overall reactivity towards C-H activation. We demonstrate this in the last section of our study.

RIXS fingerprints of spectator ligand effects in C-H activation

It has previously been demonstrated using NMR spectroscopy and time-resolved IR spectroscopy how differences in the spectator ligands of transition-metal complexes effectuate the propensity of different σ -complexes towards C-H activation (13). Following this approach, we recently reported trends in orbital energies and hybridization of unoccupied orbitals, which determine the varying reactivity towards C-H activation for two different σ -complexes, CpRhCO-octane and Rh(acac)(CO)-octane (18) (where acac = acetylacetonate). Similar to CpRh(CO)₂, the formation of the Rh(acac)(CO)-octane σ -complex follows CO dissociation from Rh(acac)(CO)₂ in octane solution. The RIXS spectrum of Rh(acac)(CO)₂ was also measured and simulated using the above-mentioned protocol and we show the agreement of simulated and measured RIXS maps in Figure S4.

In contrast to the CpRhCO-octane σ -complex, Rh(acac)(CO)-octane constitutes a particularly stable σ -complex that does not facilitate C-H activation (38). Here, we trace these observations back to changes in the occupied orbitals. In Figure 5(a) and (b), the RIXS difference maps for the two σ -complexes Rh(acac)(CO)-octane and CpRhCO-octane are shown. As can be seen, the d_{yz} RIXS peak (HOMO-

LUMO $4d_{yz} \rightarrow 4d_{xy}$ transition) in Rh(acac)(CO)-octane is merged at high energies with the other (d_z^2 , d_{xz} and $d_{x^2-y^2}$) RIXS peaks. For CpRhCO-octane, it is instead clearly separated at an energy of slightly more than 2 eV. This observation is even more apparent in the cuts through the RIXS difference maps at the respective XAS pre-edges in Figure 5(c). The higher HOMO-LUMO $4d_{yz} \rightarrow 4d_{xy}$ transition energy in Rh(acac)(CO)-octane compared to CpRhCO-octane is due to stronger C-H σ to Rh $4d_{xy}$ charge back-donation, leading to greater destabilization of the LUMO in Rh(acac)(CO)-octane compared to CpRhCO-octane and a greater stabilization of HOMO in Rh(acac)(CO)-octane than in CpRhCO-octane. This stabilization of the HOMO correlates with decreased hybridization of Rh $4d_{yz}$ with the σ^* orbital of the C-H group in Rh(acac)(CO)-octane and hence a frustrated Rh $4d_{yz}$ to C-H σ^* charge back-donation. We also note that the integrated intensity of all d_{yz} , d_z^2 , d_{xz} , and $d_{x^2-y^2}$ RIXS peaks is higher in Rh(acac)(CO)-octane compared to CpRhCO-octane, indicating increased Rh 4d character of HOMO-1, HOMO-2 and HOMO-3. This reflects the more ionic complex Rh(acac)(CO)-octane (18) with a higher effective oxidation of the Rh(I) center compared to CpRh(CO)-octane. In our previous study based on XAS (18), we established that C-H σ to Rh $4d_{xy}$ donation is stronger in Rh(acac)(CO)-octane compared to CpRhCO-oct, thereby contributing to a more stable σ -complex. Using RIXS, we extend this notion here by establishing that the Rh $4d_{yz}$ to C-H σ^* charge back-donation is also frustrated in Rh(acac)(CO)-octane and that the reduced hybridization with the C-H σ^* orbital contributes to preventing C-H activation in the Rh(acac)(CO)-octane σ -complex.

Conclusion

By simulating the valence-to core resonant inelastic X-ray scattering (VtC-RIXS) signatures at the transition metal L-edge for various key intermediates in a photochemical C-H activation reaction with a transition metal complex, we have predicted how VtC-RIXS can be used to dissect and understand the decisive orbital interactions which drive the reaction. By comparing to experimental VtC-RIXS data of CpRh(CO)₂, a well-studied model system, we were able to benchmark and validate the accuracy of our computational predictions with TD-DFT. Since C-H activation by CpRh(CO)₂ is mainly governed by electronic effects, spectroscopic signatures could be assigned to the changes in covalent interactions such as charge donation and back-donation across the reaction pathway without interference of other (e.g. steric) effects. This allows to extend the established correlation diagram for the oxidative addition step in the C-H activation process by including changes in covalency over the full 4d manifold. These changes were directly extracted from the changes in energies and intensities of VtC-RIXS peaks, which reflect the evolving character of the relevant occupied and unoccupied Rh 4d orbitals.

A robust theoretical description of how VtC-RIXS probes the evolution of valence orbitals and as such, molecular bonds, during chemical reactions constitutes a critical step towards the experimental realization of such investigations. With RIXS being an extremely photon-hungry technique, particularly in the VtC regime, time-resolved experiments have thus far been challenging or outright unfeasible even at intense X-ray free-electron laser sources. However, with already or soon-to-be operating X-ray free-electron lasers like the European XFEL (Hamburg, Germany) and the LCLS-II (Stanford, USA), which provide kHz-MHz repetition rates and thus orders of magnitude increases in average X-ray flux compared to other X-ray free-electron laser sources (39), VtC-RIXS experiments as proposed here will become routinely feasible. We anticipate future studies with time-resolved VtC-RIXS at transition metal L-edges to yield unique information on the evolution of frontier-orbital interactions in a range of photochemical and photocatalytic reactions in solution. The resulting experimental extraction and verification of orbital correlation diagrams will reveal how covalent metal-ligand interactions drive catalytic function.

Materials and Methods

Computational Details. The quantum chemical computations were performed using the ORCA program package (40) and Open-MOLCAS (41). All the geometries were optimized at the TPSSh/def2-TZVP level of theory (42, 43) followed by frequency computations. No imaginary normal modes were found confirming that the optimized structures are intermediates in the reaction pathway. Solvent effects were taken into account by incorporating the CPCM polar continuum model with hexane as the solvent (44) for all computation done in ORCA. XAS and VtC RIXS spectra were computed in ORCA using the restricted orbital subspace TD-DFT method (36) within Tamm-Damcoff approximation (45). Second order relativistic effects were taken into account using the ZORA method (46). The SARC-ZORA-TZVPP basis set was used for the Rh atom and ZORA-def2-TZVPP for the rest of the atoms (47). The three Rh 2p orbitals were rotated into the restricted orbital subspace, which also consisted of 20

occupied orbitals and 20 unoccupied orbitals. The core-excited states (intermediate states) and valence-excited states (final states) were computed by considering excitations from the occupied orbital subspace (20+3 orbitals) into the 20 selected unoccupied orbitals. All the transition dipole moments for excitations from the ground state to core-excited states and the decay from core-excited states to valence-excited states were computed using the Multi-Wfn program package (48).

The RIXS intensities were computed using the Kramer-Heisenberg formula. The discrete intensities were convoluted along the incident energy axis with a Voigt profile consisting of a 1.9 eV FWHM Lorentzian function to account for the core-hole lifetime (49) and a Gaussian function of 0.6 eV FWHM. On the energy transfer axis, the intensities were broadened with Gaussian of 0.7 eV FWHM. A shift of -22.2 eV in the incident energy axis was applied to the calculated spectrum of CpRh(CO)₂ to align it with experimental spectrum. The same shift was applied to all other calculated species reproducing relative shifts determined experimentally (18).

RIXS calculations for the different species were also carried out at the Restricted Active Space Perturbation Theory (RASPT2) level of theory (50, 51) in Open-MOLCAS. For the RASPT2 computations, the Douglas-Kroll-Hess-Hamiltonian (52) was used to account for the zeroth order relativistic effect along with Sapporo-DKH3-DZP-2012 (53) basis set for Rh and the cc-pVDZ-DK basis set (54) for all other atoms. We used three 2p orbitals with six electrons in the RAS1 space for all the species. The RAS2 space was varied accordingly for different species. We used 10 electrons in 10 orbitals in the RAS2 space for computing the RIXS maps for CpRh(CO)₂ and 10 electrons in 8 orbitals for CpRhCO. For CpRhCO-octane and CpRhCO-R-H, the RAS2 orbitals consisted of 10 electrons in 9 orbitals. A total of 50 singlet ground and valence-excited states were solved using state-averaging. A total of 40 core-excited states were solved using the HEXS keyword in RASSCF (55). Subsequently, RASPT2 computations were performed to account for dynamical correlation. The discrete transitions were convoluted in the same way as described earlier for TD-DFT. The spectra are again shifted by -67.1 eV in the incident energy axis. Unlike in TD-DFT, this constant shift does not consistently reproduce the relative shifts determined from experiment (18) for RASPT2. The RASPT2 spectra are shown in Figure S5-S8 in the Supporting Information.

Experimental Details. The VtC-RIXS experiments were performed using the AlvrA instrument of the Swiss Free Electron Laser (SwissFEL). CpRh(CO)₂ was purchased from HetCat, Rh(acac)(CO)₂ from Sigma-Aldrich. The samples were dissolved at 20 mM concentration in decane and octane, respectively (purchased from Sigma-Aldrich). The sample was delivered into the experimental chamber via a cylindrical liquid jet with a diameter of 75 μm. The sample was collected by a catcher system below the interaction zone and recirculated into the sample reservoir. The experimental chamber was kept under 500 mbar He atmosphere to minimize X-ray scattering noise and increase the X-ray transmission. The incidence energy of the X-rays was tuned across the Rh L₃-edge between 2995 eV and 3015 eV using a Si(111) monochromator with a bandwidth of ~0.4 eV. The X-ray focus spot size was ~20 x 20 μm² on the sample.

The VtC-RIXS data was collected in parallel to time-resolved experiments at a repetition rate of 100 Hz. To only include steady-state data, every second XFEL shot impinging on the sample was selected for the current analysis, thus reducing the effective repetition rate to 50 Hz. The data was recorded using a von-Hamos type X-ray emission spectrometer equipped with a 250 mm cylindrically bent Si(111) segmented crystal and a Jungfrau 4.5M detector. The energy axis of the spectrometer was calibrated with respect to the elastic scattering. The energy resolution of the spectrometer was ~0.8 eV as determined by fitting the elastic scattering below the absorption onset at 2995 eV. Each pixel of the raw single-shot Jungfrau images was corrected for pedestal levels and gains before retrieving the deposited energy in keV (56, 57). Low and high energy thresholds of 2.0 and 10.0 keV, respectively, were applied for each pixel to minimize noise and eliminate unphysical counts. In order to enhance further the signal-to-noise of the VtC-X-ray emission line, two regions of interest (ROIs) were selected on the 2D detector and subtracted from each other. The first (signal) was placed around the VtC line, whereas the second one (background) was located at the same position along the dispersive axis but offset along the non-dispersive axis.

Acknowledgments

We acknowledge the Paul Scherrer Institut, Villigen, Switzerland for provision of beamtime at the AlvrA beamline of SwissFEL. The computations were partly enabled by resources provided by the Swedish

National Infrastructure for Computing (SNIC) at UPPMAX partially funded by the Swedish Research Council through grant agreement no. 2021-22968 and 2022-22975. The computations were also partly enabled by resources provided by the National Academic Infrastructure for Supercomputing in Sweden (NAISS) and the Swedish National Infrastructure for Computing (SNIC) at NSC and PDC partially funded by the Swedish Research Council through grant agreement no. 2022/1-14, 2023/1-8, 2022-06725 and no. 2018-05973. M.O. acknowledges funding from the Swedish Research Council (grant agreement no. 2021-04521). A.B. and P.W. acknowledge funding from the Carl Tryggers Foundation (contract CTS 19:399). P.W. acknowledges funding from the Swedish Research Council (grant agreement no. 2019-04796). J.H. and N.H. acknowledge funding from the Cluster of Excellence "CUI: Advanced Imaging of Matter" of the Deutsche Forschungsgemeinschaft (DFG), EXC 2056, project ID 390715994. R.-P.W. acknowledges funding from the German Ministry of Education and Research (BMBF), project ID 05K19GU2. V.K., A.K., and C.B. acknowledge support from the Swiss National Science Foundation (SNSF) through the NCCR:MUST. A.W. acknowledges the National Science Centre, Poland (NCN), for partial support through grant no. 2019/03/X/ST3/00035.

Author Contributions: A.B., R.M.J. and P.W. originated the project concept. A.B., M.C. and M.O. performed the theoretical calculations. A.B., R.M.J, M.O. and P.W. analyzed the computational results. R.M.J., T.L., R.-P.W., J.H., R.S., E.B., V.K., A.K., A.W., D.O., C.A., C. M., P.J.M.J., C.C., C.B., N.H. and P.W. planned and executed the experiments. R.M.J., T.L., and C.C. analyzed the experimental data. A.B. R.M.J. and P.W. wrote the paper with input from all the authors.

Competing Interest Statement: The authors declare no competing interest.

References

1. K. I. Goldberg, A. S. Goldman, Large-Scale Selective Functionalization of Alkanes. *Acc. Chem. Res.* **50**, 620–626 (2017).
2. B. A. Arndtsen, R. G. Bergman, T. A. Mobley, T. H. Peterson, Selective Intermolecular Carbon-Hydrogen Bond Activation by Synthetic Metal Complexes in Homogeneous Solution. *Acc. Chem. Res.* **28**, 154–162 (1995).
3. A. J. Lees, A. A. Purwoko, Photochemical mechanisms in intermolecular C-H bond activation reactions of organometallic complexes. *Coord. Chem. Rev.* **132**, 155–160 (1994).
4. C. Jia, T. Kitamura, Y. Fujiwara, Catalytic Functionalization of Arenes and Alkanes via C-H Bond Activation. *Acc. Chem. Res.* **34**, 633–639 (2001).
5. C. P. Lenges, M. Brookhart, Addition of Olefins to Aromatic Ketones Catalyzed by Rh(I) Olefin Complexes. *J. Am. Chem. Soc.* **121**, 6616–6623 (1999).
6. S. Murai, *et al.*, Efficient catalytic addition of aromatic carbon-hydrogen bonds to olefins. *Nature* **366**, 529–531 (1993).
7. T. Matsubara, N. Koga, D. G. Musaev, K. Morokuma, Density Functional Study on Activation of *ortho*-CH Bond in Aromatic Ketone by Ru Complex. Role of Unusual Five-Coordinated d^6 Metallacycle Intermediate with Agostic Interaction. *J. Am. Chem. Soc.* **120**, 12692–12693 (1998).
8. M. Brookhart, M. L. H. Green, G. Parkin, Agostic interactions in transition metal compounds. *Proc. Natl. Acad. Sci.* **104**, 6908–6914 (2007).
9. K. M. Altus, J. A. Love, The continuum of carbon–hydrogen (C–H) activation mechanisms and terminology. *Commun. Chem.* **4**, 173 (2021).
10. J. Y. Saillard, R. Hoffmann, Carbon-hydrogen and hydrogen-hydrogen activation in transition metal complexes and on surfaces. *J. Am. Chem. Soc.* **106**, 2006–2026 (1984).
11. E. A. Cobar, R. Z. Khaliullin, R. G. Bergman, M. Head-Gordon, Theoretical study of the

- rhodium alkane interaction in transition metal alkane π -complexes. *Proc. Natl. Acad. Sci.* **104**, 6963–6968 (2007).
12. D. H. Ess, W. A. Goddard, R. A. Periana, Electrophilic, Ambiphilic, and Nucleophilic C–H Bond Activation: Understanding the Electronic Continuum of C–H Bond Activation Through Transition-State and Reaction Pathway Interaction Energy Decompositions. *Organometallics* **29**, 6459–6472 (2010).
 13. G. E. Ball, *et al.*, A delicate balance of complexation vs. activation of alkanes interacting with [Re(Cp)(CO)(PF₃)₃] studied with NMR and time-resolved IR spectroscopy. *Proc. Natl. Acad. Sci.* **104**, 6927–6932 (2007).
 14. S. E. Bromberg, *et al.*, The mechanism of a C–H bond activation reaction in room-temperature alkane solution. *Science (80-.)*. **278**, 260–263 (1997).
 15. E. P. Wasserman, C. B. Moore, R. G. Bergman, Gas-Phase Rates of Alkane C–H Oxidative Addition to a Transient CpRh(CO) Complex. *Science (80-.)*. **255**, 315–318 (1992).
 16. M. W. George, *et al.*, Understanding the factors affecting the activation of alkane by Cp’Rh(CO)₂ (Cp’ = Cp or Cp*). *Proc. Natl. Acad. Sci.* **107**, 20178–20183 (2010).
 17. A. J. Cowan, *et al.*, Time-resolved infrared (TRIR) study on the formation and reactivity of organometallic methane and ethane complexes in room temperature solution. *Proc. Natl. Acad. Sci.* **104**, 6933–6938 (2007).
 18. R. M. Jay, *et al.*, Tracking C–H activation with orbital resolution. *Science (80-.)*. **380**, 955–960 (2023).
 19. R. M. Jay, K. Kunnus, P. Wernet, K. J. Gaffney, Capturing Atom-Specific Electronic Structural Dynamics of Transition-Metal Complexes with Ultrafast Soft X-Ray Spectroscopy. *Annu. Rev. Phys. Chem.* **73**, 187–208 (2022).
 20. P. Wernet, *et al.*, Orbital-specific mapping of the ligand exchange dynamics of Fe(CO)₅ in solution. *Nature* **520**, 78–81 (2015).
 21. R. K. Hocking, *et al.*, Fe L-edge X-ray absorption spectroscopy of low-spin heme relative to non-heme Fe complexes: Delocalization of Fe d-electrons into the porphyrin ligand. *J. Am. Chem. Soc.* **129**, 113–125 (2007).
 22. H. Lim, *et al.*, K β X-ray Emission Spectroscopy of Cu(I)-Lytic Polysaccharide Monooxygenase: Direct Observation of the Frontier Molecular Orbital for H₂O₂ Activation. *J. Am. Chem. Soc.* (2023) <https://doi.org/10.1021/jacs.3c04048>.
 23. N. Lee, T. Petrenko, U. Bergmann, F. Neese, S. DeBeer, Probing Valence Orbital Composition with Iron K β X-ray Emission Spectroscopy. *J. Am. Chem. Soc.* **132**, 9715–9727 (2010).
 24. R. M. Jay, *et al.*, The nature of frontier orbitals under systematic ligand exchange in (pseudo-)octahedral Fe(II) complexes. *Phys. Chem. Chem. Phys.* **20**, 27745–27751 (2018).
 25. R. M. Jay, *et al.*, Disentangling Transient Charge Density and Metal-Ligand Covalency in Photoexcited Ferricyanide with Femtosecond Resonant Inelastic Soft X-ray Scattering. *J. Phys. Chem. Lett.* **9**, 3538–3543 (2018).
 26. E. Biasin, *et al.*, Revealing the bonding of solvated Ru complexes with valence-to-core resonant inelastic X-ray scattering. *Chem. Sci.* **12**, 3713–3725 (2021).
 27. D. R. Nascimento, *et al.*, Resonant Inelastic X-ray Scattering Calculations of Transition Metal Complexes Within a Simplified Time-Dependent Density Functional Theory Framework. *J. Chem. Theory Comput.* **17**, 3031–3038 (2021).

28. K. Kunnus, *et al.*, Viewing the Valence Electronic Structure of Ferric and Ferrous Hexacyanide in Solution from the Fe and Cyanide Perspectives. *J. Phys. Chem. B* **120**, 7182–7194 (2016).
29. J. B. Asbury, H. N. Ghosh, J. S. Yeston, R. G. Bergman, T. Lian, Sub-picosecond IR study of the reactive intermediate in an alkane C-H bond activation reaction by CpRh(CO)₂. *Organometallics* **17**, 3417–3419 (1998).
30. M. C. Asplund, *et al.*, Ultrafast UV pump/IR probe studies of C-H activation in linear, cyclic, and aryl hydrocarbons. *J. Am. Chem. Soc.* **124**, 10605–10612 (2002).
31. A. L. Pitts, *et al.*, Carbon-hydrogen activation of cycloalkanes by cyclopentadienylcarbonylrhodium-A lifetime enigma. *J. Am. Chem. Soc.* **136**, 8614–8625 (2014).
32. A. J. Rest, I. Whitwell, W. A. G. Graham, J. K. Hoyano, A. D. McMaster, Photoactivation of methane by η⁵-cyclopentadienyl and substituted η⁵-cyclopentadienyl Group 8 metal dicarbonyl complexes, [M(η⁵-C₅R₅)(CO)₂](M = Rh or Ir, R = H or Me), and dicarbonyl(η⁵-indenyl)iridium: a matrix isolation study. *J. Chem. Soc., Dalt. Trans.* **0**, 1181–1190 (1987).
33. A. A. Bengali, *et al.*, Activation of carbon-hydrogen bonds in alkanes and other organic molecules by Ir(I), Rh(I) and Ir(III) complexes. *Pure Appl. Chem.* **67**, 281–288 (1995).
34. S. T. Belt, F. W. Grevels, W. E. Klotzbuecher, A. McCamley, R. N. Perutz, Intermediates in the time-resolved and matrix photochemistry of (η⁵-cyclopentadienyl)rhodium complexes. Roles of alkane activation and rhodium-rhodium bond formation. *J. Am. Chem. Soc.* **111**, 8373–8382 (1989).
35. N. Gorgas, A. J. P. White, M. R. Crimmin, Cooperative C–H Bond Activation by a Low-Spin d⁶ Iron–Aluminum Complex. *J. Am. Chem. Soc.* **144**, 8770–8777 (2022).
36. V. Vaz da Cruz, S. Eckert, A. Föhlisch, TD-DFT simulations of K-edge resonant inelastic X-ray scattering within the restricted subspace approximation. *Phys. Chem. Chem. Phys.* **23**, 1835–1848 (2021).
37. R. Hoffmann, Building Bridges Between Inorganic and Organic Chemistry(Nobel Lecture). *Angew. Chemie Int. Ed. English* **21**, 711–724 (1982).
38. T. P. Dougherty, W. T. Grubbs, E. J. Heilweil, Photochemistry of Rh(CO)₂(acetylacetonate) and related metal dicarbonyls studied by ultrafast infrared spectroscopy. *J. Phys. Chem.* **98**, 9396–9399 (1994).
39. R. Schoenlein, *et al.*, Recent advances in ultrafast X-ray sources. *Philos. Trans. R. Soc. A Math. Phys. Eng. Sci.* **377**, 20180384 (2019).
40. F. Neese, Software update: The ORCA program system—Version 5.0. *WIREs Comput. Mol. Sci.* **12**, 1–15 (2022).
41. F. Aquilante, *et al.*, Modern quantum chemistry with [Open]Molcas. *J. Chem. Phys.* **152** (2020).
42. J. Tao, J. P. Perdew, V. N. Staroverov, G. E. Scuseria, Climbing the Density Functional Ladder: Nonempirical Meta-Generalized Gradient Approximation Designed for Molecules and Solids. *Phys. Rev. Lett.* **91**, 146401 (2003).
43. F. Weigend, R. Ahlrichs, Balanced basis sets of split valence, triple zeta valence and quadruple zeta valence quality for H to Rn: Design and assessment of accuracy. *Phys. Chem. Chem. Phys.* **7**, 3297–3305 (2005).
44. M. Cossi, N. Rega, G. Scalmani, V. Barone, Polarizable dielectric model of solvation with

- inclusion of charge penetration effects. *J. Chem. Phys.* **114**, 5691–5701 (2001).
45. S. Hirata, M. Head-Gordon, Time-dependent density functional theory within the Tamm–Dancoff approximation. *Chem. Phys. Lett.* **314**, 291–299 (1999).
 46. E. van Lenthe, E. J. Baerends, J. G. Snijders, Relativistic regular two-component Hamiltonians. *J. Chem. Phys.* **99**, 4597–4610 (1993).
 47. J. D. Rolles, F. Neese, D. A. Pantazis, All-electron scalar relativistic basis sets for the elements Rb–Xe. *J. Comput. Chem.* **41**, 1842–1849 (2020).
 48. T. Lu, F. Chen, Multiwfn: A multifunctional wavefunction analyzer. *J. Comput. Chem.* **33**, 580–592 (2012).
 49. J. L. Campbell, T. Papp, Widths of the atomic K-N7 levels. *At. Data Nucl. Data Tables* **77**, 1–56 (2001).
 50. P. Å. Malmqvist, B. O. Roos, The CASSCF state interaction method. *Chem. Phys. Lett.* **155**, 189–194 (1989).
 51. P. Å. Malmqvist, K. Pierloot, A. R. M. Shahi, C. J. Cramer, L. Gagliardi, The restricted active space followed by second-order perturbation theory method: Theory and application to the study of CuO₂ and Cu₂O₂ systems. *J. Chem. Phys.* **128**, 204109 (2008).
 52. M. Reiher, O. Salomon, B. Artur Hess, Reparameterization of hybrid functionals based on energy differences of states of different multiplicity. *Theor. Chem. Accounts Theory, Comput. Model. (Theoretica Chim. Acta)* **107**, 48–55 (2001).
 53. T. Noro, M. Sekiya, T. Koga, Segmented contracted basis sets for atoms H through Xe: Sapporo-(DK)-nZP sets (n = D, T, Q). *Theor. Chem. Acc.* **131**, 1124 (2012).
 54. W. A. de Jong, R. J. Harrison, D. A. Dixon, Parallel Douglas–Kroll energy and gradients in NWChem: Estimating scalar relativistic effects using Douglas–Kroll contracted basis sets. *J. Chem. Phys.* **114**, 48 (2001).
 55. M. G. Delcey, L. K. Sørensen, M. Vacher, R. C. Couto, M. Lundberg, Efficient calculations of a large number of highly excited states for multiconfigurational wavefunctions. *J. Comput. Chem.* **40**, 1789–1799 (2019).
 56. S. Redford, *et al.*, First full dynamic range scan of the JUNGFRU detector performed at an XFEL with an accurate intensity reference. *J. Instrum.* **15**, C02025–C02025 (2020).
 57. A. Mozzanica, *et al.*, The JUNGFRU Detector for Applications at Synchrotron Light Sources and XFELs. *Synchrotron Radiat. News* **31**, 16–20 (2018).

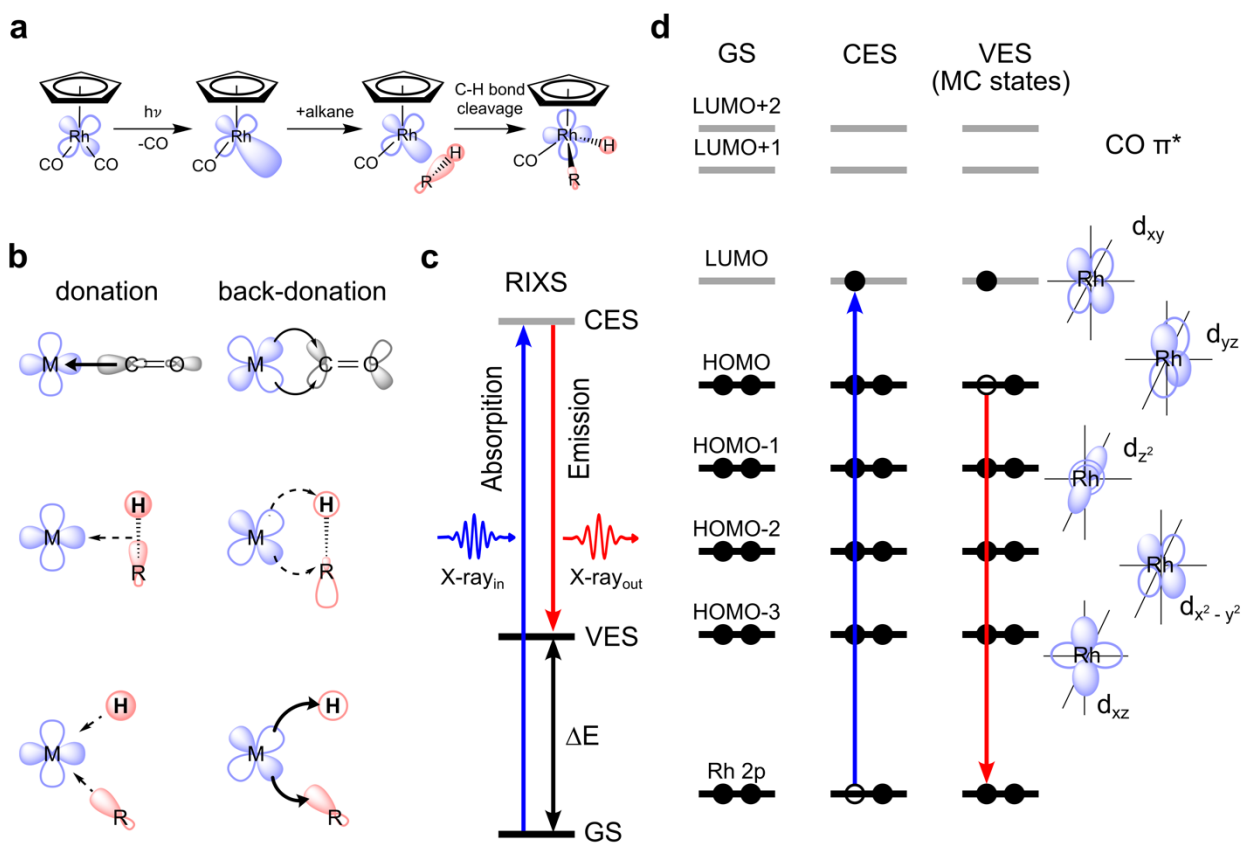


Figure 1. Metal-ligand orbital interactions in photoinitiated C-H bond activation by $\text{CpRh}(\text{CO})_2$ probed using VtC-RIXS. (a) Schematic depiction of the key intermediates and reaction steps in photo-initiated C-H activation by $\text{CpRh}(\text{CO})_2$. (b) Conceptual depiction of charge donation and back-donation interactions between the metal (M) and one ligand in the original M-CO configuration, in the M-alkane σ -complex configuration and in the final M-C-H metal hydride product (arrows denote the direction of charge transfer interaction, their thicknesses indicate the proposed relative strengths of the charge transfer). (c) State picture of the RIXS process (total energy many-electron picture), with excitation from the initial ground state (GS) to the intermediate core-excited state (CES) with incident photon energy $X\text{-ray}_{\text{in}}$ and inelastic scattering to the final valence-excited state (VES) with the measured scattered photon energy $X\text{-ray}_{\text{out}}$ and the resulting energy transfer ΔE . (d) Corresponding orbital picture (orbital energy one-electron picture) where a Rh 2p electron is promoted to a vacant molecular orbital (here of Rh 4d character) via a $2p \rightarrow 4d$ transitions, followed by transition of an electron from an occupied 4d orbital to fill the hole on the 2p orbital (via $4d \rightarrow 2p$ transitions), creating the metal-centered (MC) d-d valence-excited final states.

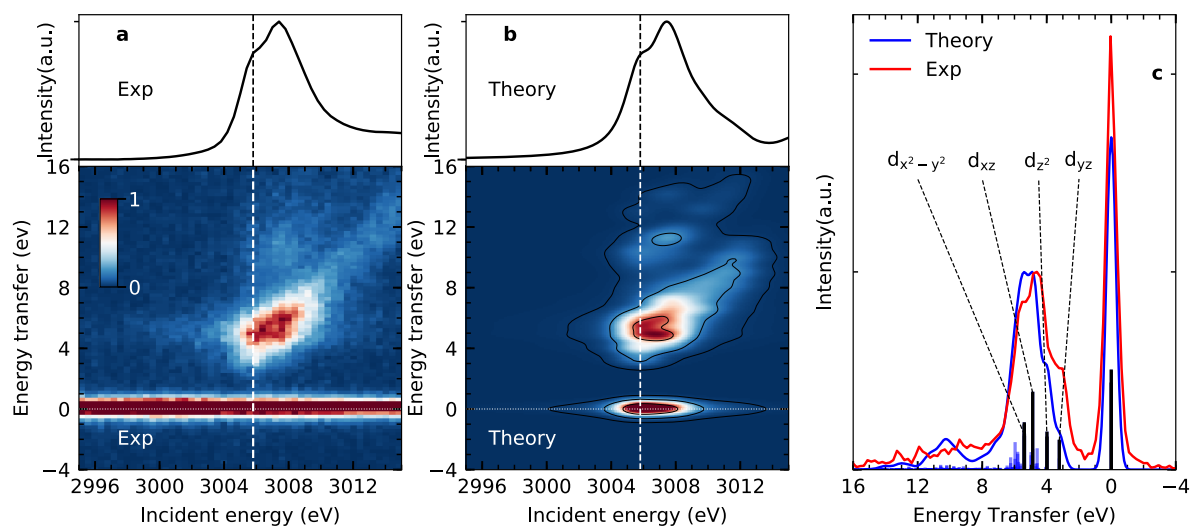


Figure 2. VtC-RIXS of $\text{CpRh}(\text{CO})_2$ as a probe of MC d-d final states. (a) Experimental Rh L-edge X-ray absorption spectrum (XAS) (top) and Rh L-edge RIXS map (bottom) for $\text{CpRh}(\text{CO})_2$. (b) Simulated Rh L-edge XAS spectrum and RIXS map at the TD-DFT level of theory. XAS spectra result from integration of RIXS intensities in a given incident-energy range along the energy-transfer axis. Vertical dashed lines in (a) and (b) indicate the energy of 3005.8 eV at which cuts were obtained to target the valence-excited MC states or, alternatively, HOMO, HOMO-1, to LUMO transitions. (c) Cuts from the experimental and simulated RIXS maps at 3005.8 eV. The dominant peaks correspond to transitions from the ground to MC states or, alternatively, to the HOMO, HOMO-1, HOMO-2, HOMO-3 ($4d_{yz}$, $4d_{z^2}$, $4d_{xz}$, and $4d_{x^2-y^2}$, respectively) to $4d_{xy}$ LUMO orbital transitions.

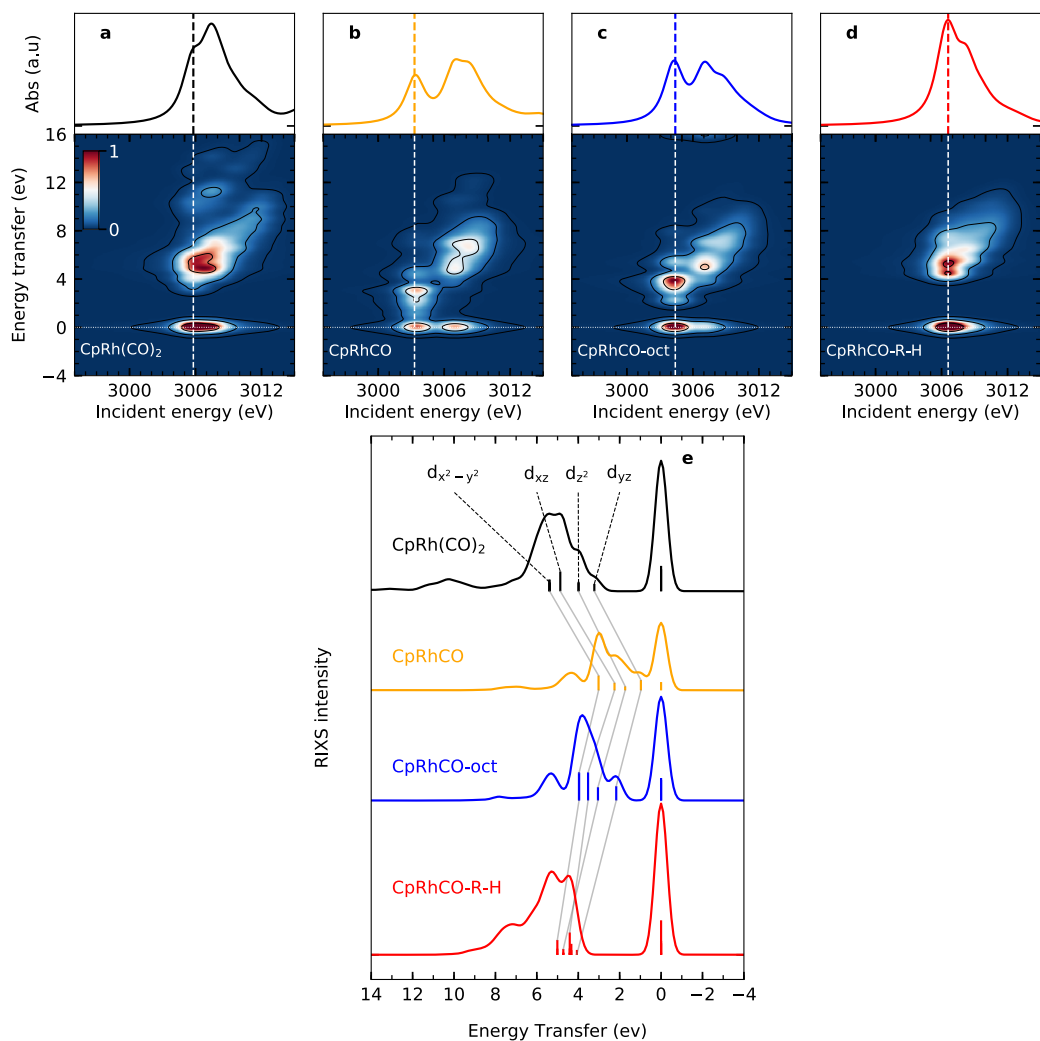


Figure 3. Simulated VtC-RIXS for key intermediates upon C-H activation in octane by $\text{CpRh}(\text{CO})_2$. Simulated Rh L_3 -edge RIXS maps for (a) $\text{CpRh}(\text{CO})_2$, (b) free fragment CpRhCO , (c) sigma-complex CpRhCO-octane (abbreviated as CpRhCO-oct) and (d) final activated product complex CpRhCO-R-H (along with the Rh L_3 -edge XAS spectra on top of the panels). (e) Cuts through the RIXS maps for the four intermediates in (a-d) at incidence energies of pre-edge excitation (indicated by the vertical lines in panels (a-d)). As in Figure 2(c), the RIXS transitions are labeled according to the involvement of the four occupied Rh 4d orbitals (gray lines connect the corresponding transitions and the evolution of their energies and intensities along the reaction pathway).

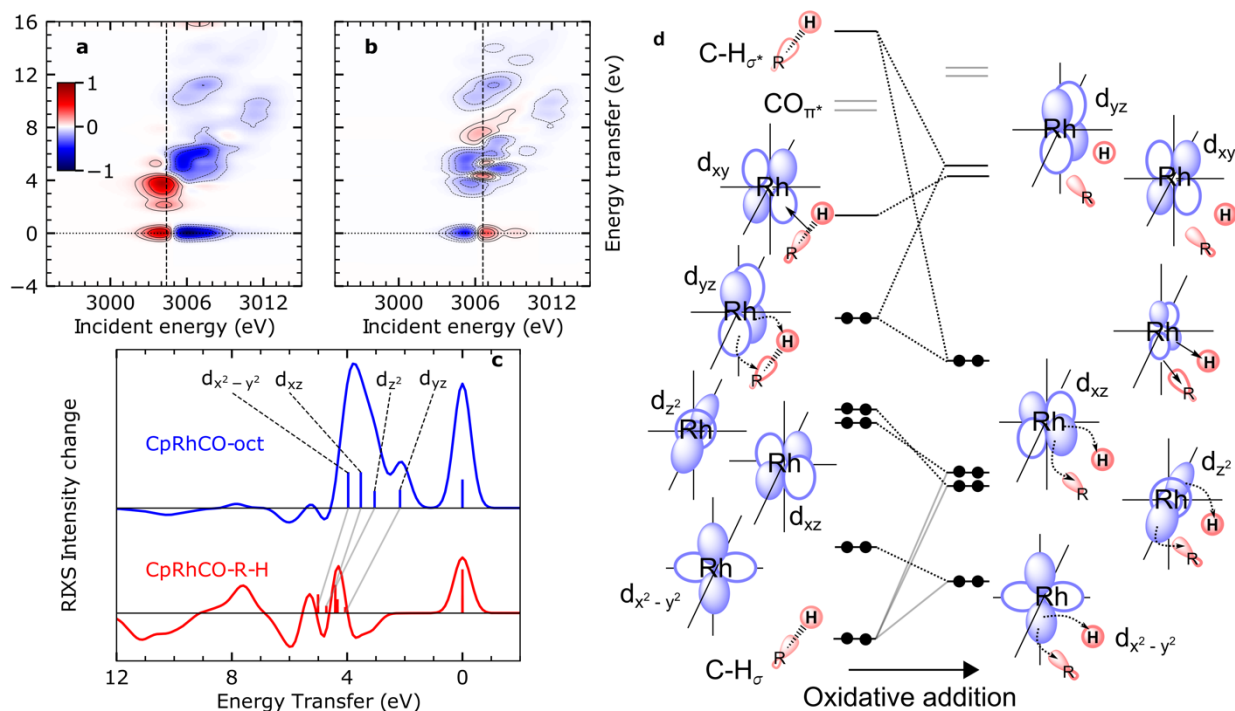


Figure 4. VtC-RIXS difference signatures for the oxidation addition step vs. the orbital correlation diagram. (a) and (b) RIXS difference maps of CpRhCO-octane and CpRhCO-R-H, respectively, obtained by subtracting the RIXS map of CpRh(CO)₂ shown in Figure 3(a) from the RIXS maps shown in Figure 3(c) and (d). Red regions denote positive intensity, blue regions denote depletion. Vertical lines indicate incidence energies where RIXS cuts were obtained. (c) Cuts in the difference RIXS maps for CpRhCO-octane (red) and CpRhCO-R-H (blue). Individual peaks are labeled by the occupied 4d orbitals as in Figures 2 and 3. Gray lines illustrate the evolution of RIXS peaks upon oxidative addition. (d) Correlation diagram as motivated and derived from interpreting the RIXS spectra for CpRhCO-octane and CpRhCO-R-H from panel (c). Dotted black lines in (d) connect the four occupied 4d orbitals in (d) as gray lines in (c) connect the corresponding RIXS peaks in (c).

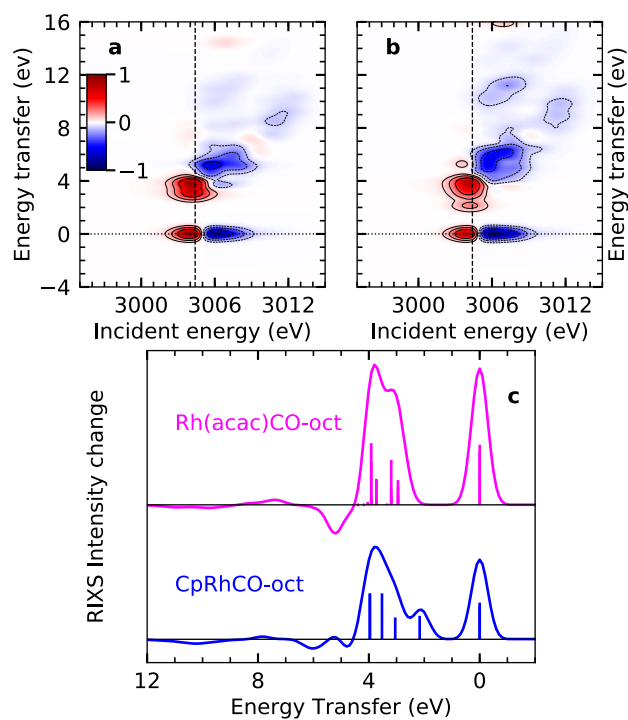


Figure 5. VtC-RIXS difference signatures as fingerprints of σ -complex reactivity. (a) Difference RIXS map of Rh(acac)(CO)-octane obtained by subtracting the calculated RIXS map of Rh(acac)(CO)₂, as shown in Figure S4 in the SI, from the calculated RIXS map of Rh(acac)(CO)-octane. (b) Difference RIXS map of CpRhCO-octane (same as in Figure 4(a)). (c) Cuts through the difference RIXS maps in (a) and (b) at the XAS pre-edge at 3004.4 eV (dashed lines in (a) and (b)) for Rh(acac)(CO)-octane (to